CrossMark
click for updates

Enhanced magnetocaloric performances and tunable martensitic transformation in $Ni_{35}Co_{15}Mn_{35-x}Fe_xTi_{15}$ all-d-metal Heusler alloys by chemical and physical pressures

Yong Li, Liang Qin, Siyuan Huang and Lingwei Li[*]

ABSTRACT The solid-state magnetic cooling (MC) method based on the magnetocaloric effect (MCE) is recognized as an environmentally friendly and high-energy-efficiency technology. The search or design of suitable magnetic materials with large MCEs is one of the main targets at present. In this work, we apply the chemical and hydrostatic pressures in the $Ni_{35}Co_{15}Mn_{35-x}Fe_xTi_{15}$ all-d-metal Heusler alloys and systematically investigate their crystal structures, phases, and magnetocaloric performances experimentally and theoretically. All the alloys are found to crystallize in an ordered B2-type structure at room temperature and the atoms of Fe are confirmed to all occupy at sites Mn(B). The total magnetic moments decrease gradually with increasing Fe content and decreasing of volume as well. The martensitic transformation temperature decreases with the increase of Fe content, whereas increases with increasing hydrostatic pressure. Moreover, obviously enhanced magnetocaloric performances can also be obtained by applied pressures. The maximum values of magnetic entropy change and refrigeration capacity are as high as $15.61(24.20) \, J \, (kg \, K)^{-1}$ and $109.91(347.26) \, J \, kg^{-1}$ with $\Delta H = 20(50) \, kOe$, respectively. These magnetocaloric performances are superior to most of the recently reported famous materials, indicating the potential application for active MC.

Keywords: magnetocaloric performances, magnetic properties, pressure effects, magnetocaloric effect, all-d-metal Heusler alloys

INTRODUCTION

In recent years, various magnetic materials with outstanding performances have been developed and attracted extensive research interest [1–8]. Among them, the solid-state magnetic cooling (MC) method based on the magnetocaloric effect (MCE) of magnetic solids has been recognized as one of the most potential promising environmentally friendly and high-efficiency alternative methods to the well-used state-of-the-art gas compression cooling technique [1–3]. The MCE is a magneto-thermodynamic response which manifests the temperature (entropy) change of magnetic solids by applying or removing the magnetic field. Thus, plenty of magnetic solids have been systematically investigated in the last thirty years, and some of them are reported to exhibit large MCEs, such as $La(Fe,Si)_{13}H_x$, selected heavy rare earth (RE)-based compounds, MnTMX (TM = Fe, Co, and Ni; X = Ge and Si), as well as NiMn-based Heusler alloys with first-order magnetostructural transitions (MSTs) [9–18]. However, a large gap between the developing of magnetocaloric materials and the active MC applications still exists at the present stage. The researchers in this field are devoting to design or search of novel magnetic materials with promising magnetocaloric performances.

Recently, a new material system with MSTs, named all-d-metal Heusler alloys, was established by modifying the p-d hybridization in the NiMn-based Heusler alloys to d-d hybridization by transition-metal elements with low valence-electrons. Various interesting physical properties and potential applications have also been realized very recently [19–28]. Strong ferromagnetic (FM) coupling and MST were established by introducing Co element in Mn-Ni-Ti [19–21]. A huge reversible elastocaloric effect (eCE) with the entropy change of $45 \, J \, (kg \, K)^{-1}$ and adiabatic temperature change (ΔT_{ad}) up to 31.5 K was obtained in MnNiTi [22]. An outstanding barocaloric effect was also gained in $Ni_{50}Mn_{31.5}Ti_{18.5}$ [23]. A large low-magnetic-field magnetic entropy change (ΔS_M) was observed in $Ni_{37}Cu_{2.5}Co_{12.5}Mn_{35}Ti_{15}$ ribbon [24]. $Ni_{37}Co_9Fe_4Mn_{35}Ti_{15}$ alloy gained maximum ΔT_{ad} of 6.3 K under a uniaxial stress of 400 MPa [25]. Meanwhile, the first principle calculations were also used to predict the stability of phase, possible martensitic transformation (MT), and electronic behaviors [29–32] for other similar alloys in all-d-metal Heusler systems. Moreover, the hydrostatic pressure is considered as a clean way to affect the atomic distance and thus change the physical properties of the materials, especially for some MST systems [33–38]. Furthermore, dual-field-induced change of physical performances has also been studied. A small thermal hysteresis (6 K) was obtained in $Ni_2Cu_{0.2}Mn_{1.2}In_{0.6}$ accompanied by maximum ΔT_{ad} (−13 K) and MT temperature (T_t) can further be tailored close to room temperature (RT) with the application of chemical and hydrostatic pressure in $Ni_2Cu_xMn_{1.4-x}In_{0.6}$ [37]. Lázpita *et al.* [38] have established a pressure-tuned Curie temperature in austenite (T_C^A) and in martensite (T_C^M) in the $Ni_{50}Mn_{34.5}In_{15.5}$.

In this work, both chemical and hydrostatic pressures are applied to tune the MST and MCE in $Ni_{35}Co_{15}Mn_{35-x}Fe_xTi_{15}$ all-d-metal Heusler alloys. The T_t shifts to a low temperature for $Ni_{35}Co_{15}Mn_{35-x}Fe_xTi_{15}$ with increasing x, i.e., the austenite is stabilized. By further applying hydrostatic pressure, T_t shifts back to a high temperature again from 196 to 236 K for

Key Laboratory of Novel Materials for Sensor of Zhejiang Province, Institute of Advanced Magnetic Materials, Hangzhou Dianzi University, Hangzhou 310018, China
* Corresponding author (email: lingwei@hdu.edu.cn)

$Ni_{35}Co_{15}Mn_{31}Fe_4Ti_{15}$. The results indicate that the magnetic field makes austenite more stable, whereas the pressure prefers to stabilize martensite. Moreover, enhanced MCE of 15.61 J (kg K)$^{-1}$ (20 kOe, 0.35 GPa) and large refrigeration capacity (RC) of 347.26 J kg^{-1} (50 kOe, 0.35 GPa) can be achieved, which are comparable to or even larger than most of reported results for magnetic refrigeration materials. The atom occupations are also discussed [39]. The present study provides a useful method to tune the MST and improve the magnetocaloric performances of the all-d-metal Heusler alloys.

EXPERIMENTAL AND SIMULATION DETAILS

The polycrystalline $Ni_{35}Co_{15}Mn_{35-x}Fe_xTi_{15}$ ($x = 2, 4, 6$) alloy ingots were all fabricated from high-purity metals (nickel (Ni, 99.995%), cobalt (Co, 99.97%), manganese (Mn, 99.95%), iron (Fe, 99.95%), and titanium (Ti, 99.995%)) by the arc-melting method under Ar gases. To ensure homogeneity, the alloy ingots were flipped and re-melted for four times. Then the $Ni_{35}Co_{15}Mn_{35-x}Fe_xTi_{15}$ ribbons were obtained by the melt spinning method with the linear speed of 15 m s^{-1} and injection pressure of 0.11 MPa. The microstructure and chemical compositions were determined by scanning electron microscope (SEM) and X-ray energy-dispersive spectroscopy (EDS) (Sigma-300, Zeiss). The crystal structure of $Ni_{35}Co_{15}Mn_{35-x}Fe_xTi_{15}$ ribbons was determined by RT X-ray diffraction (XRD, SmartLab-9kW, Rigaku). The magnetization data for $Ni_{35}Co_{15}Mn_{35-x}Fe_xTi_{15}$ were obtained by using a magnetic property measurement system (MPMS3, Quantum Design). Hydrostatic pressure was applied to the ribbon with a Be-Cu cylinder cell as the pressurized module. The standard sample of Pb and measured ribbon were encapsulated in a Teflon tube which was dfilled with oil (daphne, 7373) as pressure transmitting media. The Teflon tube was put into the channel of the pressure cell. The value of hydrostatic pressure was confirmed by measuring the well-known superconducting transition temperature of Pb. The atomic site occupation, lattice constants, and magnetic properties at the ground state of $Ni_{35}Co_{15}Mn_{35-x}Fe_xTi_{15}$ alloys in cubic austenite were calculated by the self-consistent Korringa-Kohn-Rostoker method combined with coherent potential approximation (KKR-CPA).

RESULTS AND DISCUSSION

The XRD patterns of $Ni_{35}Co_{15}Mn_{35-x}Fe_xTi_{15}$ ($x = 2, 4, 6$) ribbons at RT are depicted in Fig. 1a. Similar to other reported all-d-metal alloys in cubic phase [15,17,21,40–42], the present three samples show ordered B2-type cubic structure and no impure phases can be observed. The miller indices of (220), (400), and (422) are indexed in the corresponding peaks. With increasing Fe content, the lattice constants, 5.893(2) Å for $x = 2$, 5.891(6) Å for $x = 4$, and 5.887(2) Å for $x = 6$, listed in Table S1, decrease gradually due to the smaller radius of Fe atom than that of Mn atom. Secondary electron images of free surface and fractured surface using SEM for $Ni_{35}Co_{15}Mn_{35-x}Fe_xTi_{15}$ are displayed in Fig. S1. The grain sizes for $x = 2$ are not uniform (Fig. S1a) and obviously larger than those for $x = 4$ (Fig. S1c) and $x = 6$ (Fig. S1e) in free surfaces. The long columnar crystals that prefer to arrange along the temperature gradient direction in the fracture surfaces are shown in Fig. S1b, d, and f, resulting from the thermodynamic principle. The EDS mapping results were taken into consideration to detect the actual composition. The results, summarized in Table S1, show the close values of five

elements between actual composition and nominal composition.

The full-potential Korringa-Kohn-Rostoker method combined with coherent potential approximation (KKR-CPA) [39] was applied to clarify the atomic site occupation in the case of substituting Mn by Fe for $Ni_{35}Co_{15}Mn_{35-x}Fe_xTi_{15}$ ($x = 0, 2, 4, 6$), as shown in Fig. S2. For the off-stoichiometric Cu$_2$MnAl-type $Ni_{50}Mn_{35}Ti_{15}$, the atomic site occupation is $(Ni_{25})_A(Mn_{25})_B$-$(Ni_{25})_C(Ti_{15}Mn_{10})_D$ according to the valence-electron site occupation rule [15]. Ni atoms with more valence electrons occupy sites A (1/4, 1/4, 1/4) and C (3/4, 3/4, 3/4), Mn atoms occupy sites B (1/2, 1/2, 1/2), Ti atoms and redundant Mn atoms occupy sites D (0, 0, 0). In the case of Ni atoms substituted by Co atoms, Co atoms may occupy either sites A or sites C or randomly. Herein, we consider different site occupations for Co atoms. For our initial composition $Ni_{35}Co_{15}Mn_{35}Ti_{15}$ ($x = 0$), the formula of alloy can be organized as $(Ni_{25-y}Co_y)_A(Mn_{25})_B(Ni_{10+y}Co_{15-y})_C$-$(Mn_{10}Ti_{15})_D$. The minimum energy at the ground state can be obtained by changing the Co content (y) at A atoms. What is noteworthy is that sites A and C are equivalent sites, and therefore, the finite y values were chosen to calculate the most stable state. As shown in Fig. S2a, the total energy (1 Ry = 13.606 eV) increases with decreasing Co content (y) at sites A and reaches a maximum when quasi-average Co content (y) locates at sites A and C. The minimum of total energy appears at $y = 15$, i.e., $(Ni_{10}Co_{15})_A(Mn_{25})_B(Ni_{25})_C(Mn_{10}Ti_{15})_D$, indicating that the Co atoms all prefer to occupy sites A or sites C. In the present work, on the basis of the atomic site occupations for $(Ni_{10}Co_{15})_A(Mn_{25})_B(Ni_{25})_C(Mn_{10}Ti_{15})_D$, we further substitute Mn atoms by Fe atoms for $Ni_{35}Co_{15}Mn_{35-x}Fe_xTi_{15}$ ($x = 2, 4, 6$). To draw analogous conclusions, the Fe atoms have more valence electrons than those of Mn and Ti atoms, but less than those of Ni and Co atoms [15,43]. Fe atoms prefer to occupy sites Mn(B)/Mn(D), and the corresponding formulas of three alloys can be organized as $(Ni_{10}Co_{15})_A(Mn_{25-z}Fe_z)_B(Ni_{25})_C(Mn_{8+z}Fe_{2-z}Ti_{15})_D$, $0 \leq z \leq 2$ in Fig. S2b, $(Ni_{10}Co_{15})_A(Mn_{25-z}Fe_z)_B(Ni_{25})_C(Mn_{6+z}Fe_{4-z}Ti_{15})_D$, $0 \leq z \leq 4$ in Fig. S2c and $(Ni_{10}Co_{15})_A(Mn_{25-z}Fe_z)_B$-$(Ni_{25})_C(Mn_{4+z}Fe_{6-z}Ti_{15})_D$, $0 \leq z \leq 6$ in Fig. S2d. The calculated lattice constants are 5.724 Å ($x = 0$), 5.720 Å ($x = 2$), 5.716 Å ($x = 4$), and 5.712 Å ($x = 6$), respectively, which decrease linearly with increasing Fe content. The total energy decreases with the increase of Fe content (z) at sites B, indicating that the introduced Fe atoms prefer to all occupy sites B, rather than sites D. The final forms of the atomic site occupations are $(Ni_{10}Co_{15})_A$-$(Mn_{23}Fe_2)_B(Ni_{25})_C(Mn_8Ti_{15})_D$, $(Ni_{10}Co_{15})_A(Mn_{21}Fe_4)_B(Ni_{25})_C$-$(Mn_8Ti_{15})_D$, $(Ni_{10}Co_{15})_A(Mn_{19}Fe_6)_B(Ni_{25})_C(Mn_8Ti_{15})_D$ for $Ni_{35}Co_{15}Mn_{35-x}Fe_xTi_{15}$ ($x = 2, 4, 6$), respectively. Therefore, the final schematic structure of atomic site occupation is depicted in Fig. 1b.

Calculated total and atomic magnetic moments are depicted in Fig. 1c and listed in Table S2. For $x = 0$, the total magnetic moment is 2.2537 μ_B, which is mainly contributed by CoA, MnB, and MnD atoms. With increasing Fe atoms at sites MnB, Mn(B)-Co(A)-Mn(D) configuration still maintains, but the magnetic moment of Fe atoms is always weaker than the magnetic moment of Co atoms. The total magnetic moment, contributed by CoA, MnB, FeB, and MnD sites, linearly decreases to 2.0703 μ_B ($x = 6$).

Besides, the effect of volume compression/expansion on magnetic moments is also considered for $Ni_{35}Co_{15}Mn_{31}Fe_4Ti_{15}$. The total and atomic magnetic moments as a function of volume change (v, %), in which v is defined as $(V_1-V_0)/V_0$, V_0 is the
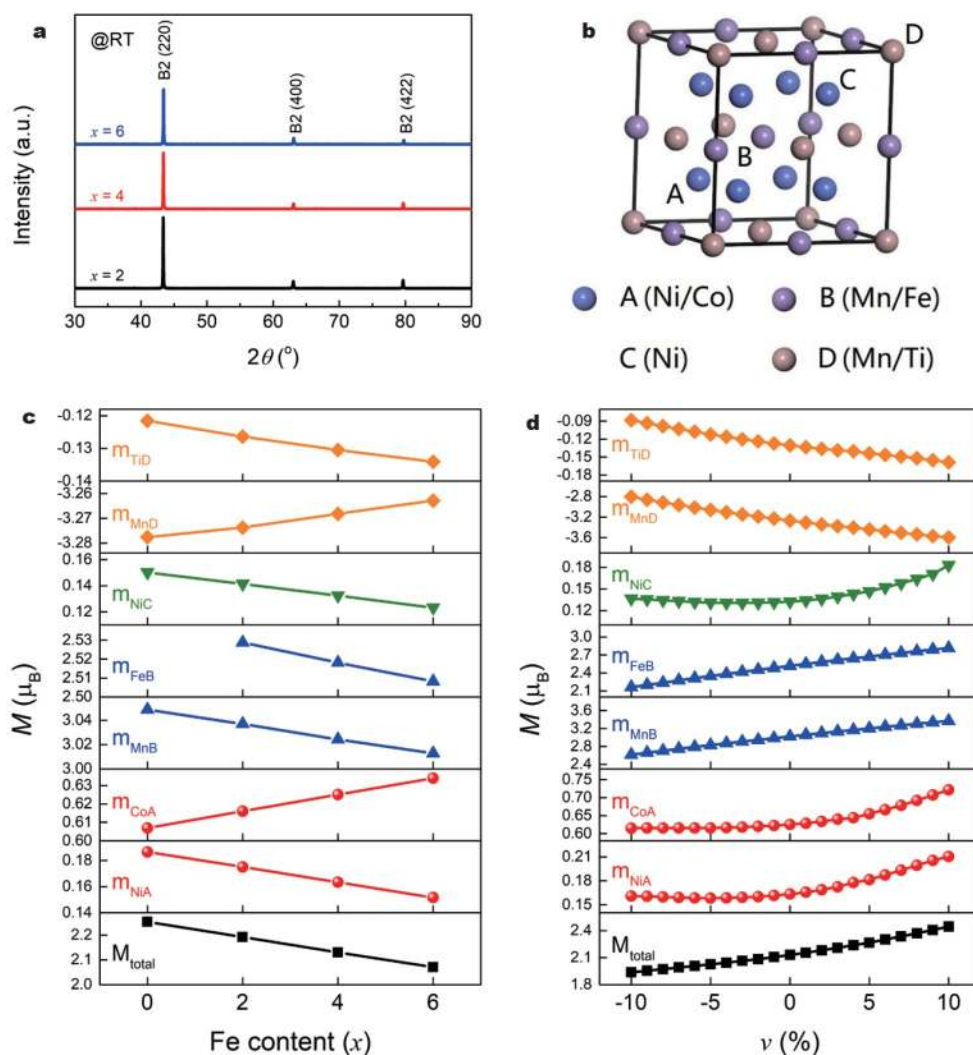
Figure 1 (a) Room-temperature XRD patterns of $Ni_{35}Co_{15}Mn_{35-x}Fe_xTi_{15}$ (x = 2, 4, 6); (b) schematic structure of $Ni_{35}Co_{15}Mn_{35-x}Fe_xTi_{15}$ (x = 2, 4, 6) and individual atomic site occupations; (c) calculated total magnetic moment and atomic magnetic moments as a function of Fe content (x) for $Ni_{35}Co_{15}Mn_{35-x}Fe_xTi_{15}$ (x = 0, 2, 4, 6); (d) calculated total magnetic moment and atomic magnetic moments as a function of volume change (v) for $Ni_{35}Co_{15}Mn_{31}Fe_4Ti_{15}$.

volume at equilibrium lattice constant, are depicted in Fig. 1d and listed in Table S3. With increasing volume, the total magnetic moment quasi-linearly increases, atomic magnetic moments increase at sites B and D, keeping basically unchanged for volume compression ($v < 0$) and increasing for volume expansion ($v > 0$) at sites A and C, owing to the varying strength of magnetic exchange interactions in the Mn(B)-Co(A)-Mn(D) configurations.

The temperature dependence of magnetization (M-T) curves under a magnetic field of 1 kOe for $Ni_{35}Co_{15}Mn_{35-x}Fe_xTi_{15}$ (x = 2, 4, 6) at ambient pressure is depicted in Fig. 2a. All the samples exhibit a similar phenomenon. In the process of cooling, a paramagnetic (PM) to FM (PM-FM) transition happens in the austenitic state, followed by the transition from FM austenite to weak-magnetic (WM) martensite. Herein, we take the first derivative of the data from Fig. 2a to obtain the values of T_C and T_t. For x = 2, the Curie temperature in austenite (T_C^A) occurs at 371 K. Subsequently, the low-temperature transitions accompanied by thermal hysteresis happen, showing that the transitions belong to first-order MST. A large magnetization change

(ΔM) is also obtained around MST which is a benefit to magnetoresponsive effect. The normal/reverse MT temperature (T_t/T_t') locates at 230 and 262 K, respectively. With increasing Fe content, the T_C^A increases, 379 K for x= 4 and 387 K for x = 6, and at the same time T_t (T_t') obviously decreases, 196 K (224 K) for x= 4 and 132 K (176 K) for x = 6. The data are listed in Table S2. It is clearly seen that introducing Fe on sites Mn(B) makes the austenitic phase more stable.

$Ni_{35}Co_{15}Mn_{31}Fe_4Ti_{15}$ was further selected to investigate the hydrostatic pressure effect on MT and magnetic properties. Fig. 2b depicts the M-T curves of $Ni_{35}Co_{15}Mn_{31}Fe_4Ti_{15}$ with the magnetic field of 1 kOe under hydrostatic pressures of 0, 0.25, 0.35, and 0.72 GPa, respectively. With increasing hydrostatic pressure, the values of T_C^A (376 K) keep basically unchanged which means that T_C^A is insensitive to hydrostatic pressure. Hence, the M-T curves are shown in the range of MT only for better clarify. At ambient pressure (P = 0 GPa), T_t (T_t') locates at 196 K (224 K) with a ΔM of 67.09 emu g^{-1}. On the one hand, T_t (T_t') listed in Table S1, 196 K (234 K) for P = 0.25 GPa, 200 K (246 K) for P = 0.35 GPa, 236 K (262 K) for P = 0.72 GPa,
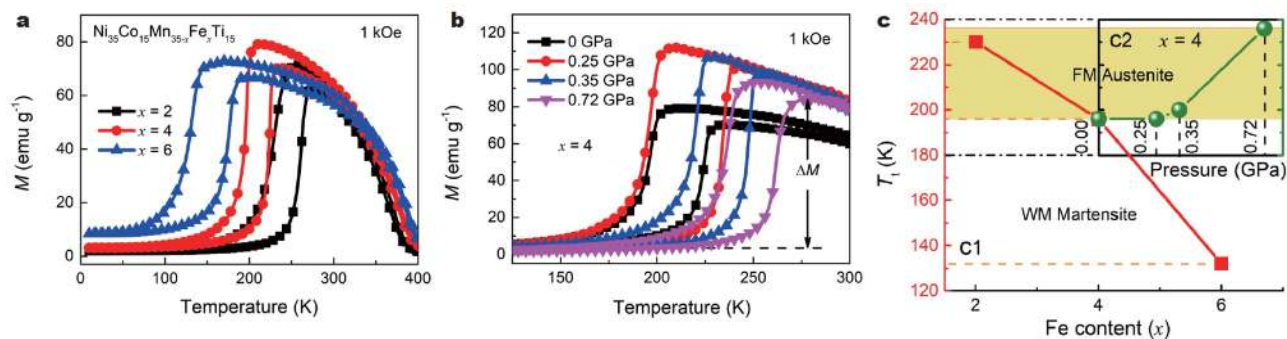
Figure 2 (a) Temperature dependence of magnetization (*M-T*) curves for $Ni_{35}Co_{15}Mn_{35-x}Fe_xTi_{15}$ ($x = 2, 4, 6$) in a magnetic field of 1 kOe; (b) temperature dependence of magnetization (*M-T*) curves for $Ni_{35}Co_{15}Mn_{31}Fe_4Ti_{15}$ in a magnetic field of 1 kOe under hydrostatic pressures of 0, 0.25, 0.35, and 0.72 GPa, respectively; (c) phase diagrams of (c1) $Ni_{35}Co_{15}Mn_{35-x}Fe_xTi_{15}$ ($x = 2, 4, 6$) and (c2) $Ni_{35}Co_{15}Mn_{31}Fe_4Ti_{15}$ under hydrostatic pressures of 0, 0.25, 0.35, and 0.72 GPa, respectively.

monotonically increases with increasing applied hydrostatic pressure, meaning that the hydrostatic pressure stabilizes the martensite due to the fact that the unit cell volume in the martensitic state is lower than that in the austenitic state [41]. Strengthening of d-d hybridization results in more thermodynamic driving force needed to make the MT occur [36,44]. On the other hand, the value of ΔM increases first at 0.25 GPa resulting from enhancement of FM interaction of Mn(B)-Co(A)-Mn(D) configuration. With further increasing hydrostatic pressure, nearest neighbor Mn(B)-Mn(D) distances decrease, and antiferromagnetic interaction of Mn(B)-Mn(D) configuration forms, which gives rise to the suppression effect of net magnetism of austenite and the declining tendency of ΔM. The large ΔM values, all above 80 emu g^{-1} under various hydrostatic pressures compared with under ambient pressure, are beneficial to the low-field MCE. The results indicate that the hydrostatic pressure can be an effective way to tailor MT and enhance magnetic responsive properties. For a better understanding of the actual influence of combined chemical and hydrostatic pressures on T_t, the structural and magnetic phase diagram is displayed, as depicted in Fig. 2c. The MST happens between FM austenite and WM martensite. The opposite influence of chemical and hydrostatic pressures on T_t can be clearly seen. In Fig. 2c1, the T_t decreases from 230 to 132 K with x increasing from 2 to 6. The introduced Fe at sites Mn(B) makes the T_t decrease, i.e., chemical pressure makes the more stable FM austenite. In Fig. 2c2, with further applying hydrostatic pressure for $x = 4$, the T_t increases from 196 K ($P = 0$ GPa) to 236 K ($P = 0.72$ GPa) with increasing hydrostatic pressure. The applied hydrostatic pressure makes the more stable WM martensite without changing composition. The results indicate that the magnetic field makes austenite more stable, whereas the pressure prefers to stabilize martensite. The decreased T_t (chemical pressure) provides wider temperature space to tailor T_t by application of hydrostatic pressure. Therefore, the combined chemical and hydrostatic pressures can control the MST of all-d-metal alloys to the desired temperature range [37].

Usually, to calculate ΔS_M based on the MST with thermal hysteresis, the temperature loop method [10,42,45,46] is used to measure isothermal magnetization curves around MST to avoid misestimating ΔS_M. Fig. S3a–c show the isothermal *M-H* curves with the magnetic field up to 70 kOe around T_t' for $Ni_{35}Co_{15}Mn_{35-x}Fe_xTi_{15}$ ($x = 2, 4, 6$) at ambient pressure. The three samples exhibit a similar metamagnetic transition process in the

region of T_t' with increasing magnetic field. At low temperatures, the low magnetization is consistent with *M-T* curves in Fig. 2a due to that the samples stay in a low temperature range with a weak magnetic state. The magnetization increases monotonously and is unsaturated up to 70 kOe. Obvious field-induced MT transition accompanied by large magnetization changes can be observed around T_t'. With increasing temperature, the critical field (H_{cr}) defined as the minimum driving field for the reverse MT declines monotonously, which is beneficial to the low-magnetic-field-induced magnetoresponsive effect. Large magnetic hysteresis from WM martensite to FM austenite upon increasing and decreasing magnetic field can also be observed. In order to better verify the transition character for magnetic-field-induced reverse MT, the Arrott plots (M^2 *vs.* H/M) of $Ni_{35}Co_{15}Mn_{35-x}Fe_xTi_{15}$ ($x = 2, 4, 6$) are shown in Fig. S3d–f, respectively. According to Banerjee's criterion [47], it belongs to the nature of first-order/second-order transition when a negative/positive slope appears. The obvious S-shape curves, i.e., the existence of a negative slope, indicate that the first-order transition occurs. Fig. S4a–c show the isothermal *M-H* curves with the application of hydrostatic pressures of 0.25, 0.35, 0.72 GPa for $Ni_{35}Co_{15}Mn_{31}Fe_4Ti_{15}$, respectively. The phenomena about weak and unsaturated magnetization curves at low temperatures, magnetic-field-induced reverse MT in the vicinity of T_t', and declined H_{cr} are similar with samples at ambient pressure. As the T_C^A is above the T_t, the parent phase with FM state shows high magnetization; the obvious difference is that the values of saturation magnetization under hydrostatic pressures are bigger than the value at ambient pressure, which is beneficial for enhancing MCE. The occurrence of negative slope from Arrott plots indicates that it still belongs to the first-order transition under hydrostatic pressures, as shown in Fig. S4d–f of 0.25, 0.35, and 0.72 GPa, respectively.

The values of ΔS_M were calculated from the isothermal magnetization data. The temperature dependence of ΔS_M using the integrated Maxwell relation [45]:

$$S_M = \int_0^H (\partial M / \partial T)_H dH,$$

with a magnetic field change (ΔH) of 70 kOe is depicted in Fig. S3a–c for $Ni_{35}Co_{15}Mn_{35-x}Fe_xTi_{15}$ ($x = 2, 4, 6$), respectively. All samples exhibit a positive ΔS_M because the martensite is a weak magnetic state and austenite is an FM state. With increasing applied magnetic field, the maximum value markedly shifts to lower temperatures which means that the magnetic field
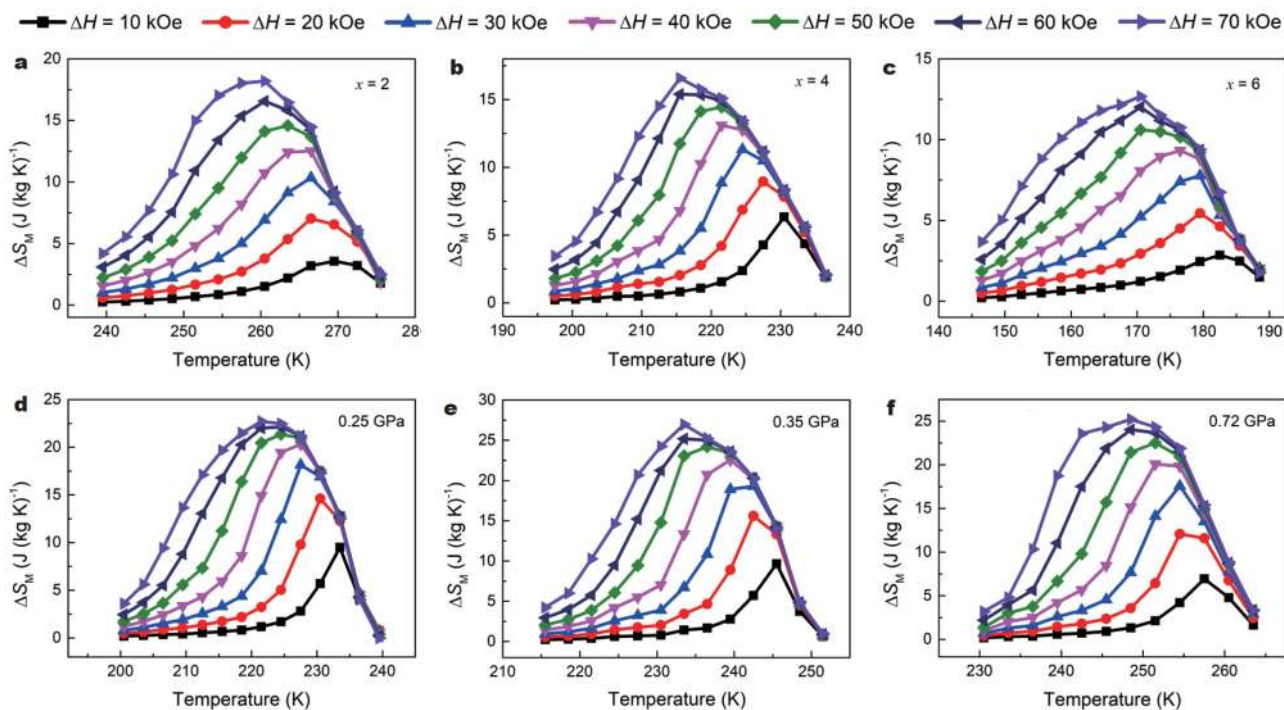
Figure 3 (a–c) ΔS_M in magnetic field change up to 70 kOe for $Ni_{35}Co_{15}Mn_{35-x}Fe_xTi_{15}$ (x = 2, 4, 6), respectively; (d–f) ΔS_M in magnetic field change up to 70 kOe for $Ni_{35}Co_{15}Mn_{31}Fe_4Ti_{15}$ (x = 4) under hydrostatic pressures of 0.25, 0.35 and 0.72 GPa, respectively.

makes T_t' decline, i.e., the magnetic field makes austenite more stable. The maximum values of ΔS_M are 7.02, 8.94, 5.44 J (kg K)$^{-1}$ with ΔH = 20 kOe and 14.58, 14.45, 10.61 J (kg K)$^{-1}$ with ΔH = 50 kOe for $Ni_{35}Co_{15}Mn_{35-x}Fe_xTi_{15}$ (x = 2, 4, 6), respectively. The influence of hydrostatic pressure on the ΔS_M is also discussed. Fig. 3d–f show ΔS_M of $Ni_{35}Co_{15}Mn_{31}Fe_4Ti_{15}$ at 0.25, 0.35, and 0.72 GPa, respectively. The magnetic field drives the maximum value to lower temperatures. The maximum value raises to high temperature compared with ambient pressure. The maximum values of ΔS_M are 14.61, 15.61, 12.07 J (kg K)$^{-1}$ with ΔH = 20 kOe and 21.35, 24.20, 22.52 J (kg K)$^{-1}$ with ΔH = 50 kOe for 0.25, 0.35, and 0.72 GPa, respectively. The data can be seen in Table S4.

Fig. 4a shows ΔS_M as a function of pressure under various magnetic field changes. Below 0.35 GPa, values of ΔS_M increase monotonously and are 14.61, 21.35 J (kg K)$^{-1}$ (0.25 GPa) and 15.61, 24.20 J (kg K)$^{-1}$ (0.35 GPa) with ΔH of 20 and 50 kOe, respectively. With further increasing hydrostatic pressure, ΔS_M decreases slightly and reaches to 12.07 and 22.52 J (kg K)$^{-1}$ (0.72 GPa) with ΔH of 20 and 50 kOe, respectively. The values of ΔS_M obviously increase at any hydrostatic pressures compared with the values at ambient pressure, indicating that application of hydrostatic pressure has a positive effect on MCE. Therefore, we can gain the maximum values (yellow area) at 0.35 GPa. Fig. 4b shows the comparison of ΔS_M between present ribbon (star) and other compounds (some conventional and all-d-metal magnetic refrigeration materials with MST, triangle) [7,8,17,19,21,24,41,46,48–50] with ΔH of 20 kOe. The value at 0.35 GPa is larger than 15.00 J (kg K)$^{-1}$ and is comparable to and even larger than the other, such as 14.00 J (kg K)$^{-1}$ for $Gd_5(Si_2Ge_2)$ [49], 14.30 J (kg K)$^{-1}$ for $LaFe_{11.4}Si_{1.6}$ [7] and 15.88 J (kg K)$^{-1}$ for $Ni_{35}Cu_{2.5}Co_{12.5}Mn_{35}Ti_{15}$ [21].

The RC, defined as

$$RC = \int_{T_1}^{T_2} |\Delta S_M| \, dT,$$

where T_1 and T_2 are the temperatures at two sides of the full width half-maximum (FWHM) in $\Delta S_M(T)$ curves, is also used to determine the magnetocaloric performance. The quasi-linear increase of RC is observed with increasing magnetic field under various applied hydrostatic pressures, as depicted in Fig. 4c. The RC value with hydrostatic pressure is larger than the original value at ambient pressure. But the RC declines at 0.72 GPa due to a smaller ΔS_M and comparative FWHM value. In the same way, the RC values of present ribbon (star) and other typical materials (triangle) are plotted in Fig. 4d [19,41,44,48,49,51–53] with ΔH of 20 kOe (solid) and 50 kOe (hollow), respectively. The values at ambient pressure of 86.68 J kg^{-1} (0–20 kOe) and 232.26 J kg^{-1} (0–50 kOe) are comparable to those of other materials, such as 80.00 J kg^{-1} for $Ni_{35}Co_{15}Mn_{35}Ti_{15}$ (0–20 kOe) [15], 91.50 J kg^{-1} for $Ni_{50}Mn_{32.7}Cu_{1.3}In_{16}$ (0–20 kOe) [51], 267.00 J kg^{-1} for $Ni_{35}Co_{15}Mn_{35}Ti_{15}$ (0–50 kOe) [15], 197.00 J kg^{-1} for $Ni_{36.0}Co_{14.0}Mn_{35.7}Ti_{14.3}$ (0–50 kOe) [48]. Encouragingly, the RC values reach 109.91 J kg^{-1} (0.25 GPa) and 347.26 J kg^{-1} (0.35 GPa), which are both larger than the materials for comparison. Thus, application of hydrostatic pressure not only tailors MT but also enhances and maintains large ΔS_M. The low driven magnetic field and near-RT atmosphere make the all-d-metal ribbon more promising for practical applications.

CONCLUSIONS
In summary, the $Ni_{35}Co_{15}Mn_{35-x}Fe_xTi_{15}$ (x = 2, 4, 6) ribbons are fabricated and systematically investigated with respect to structure, phase transformation, and magnetocaloric performances
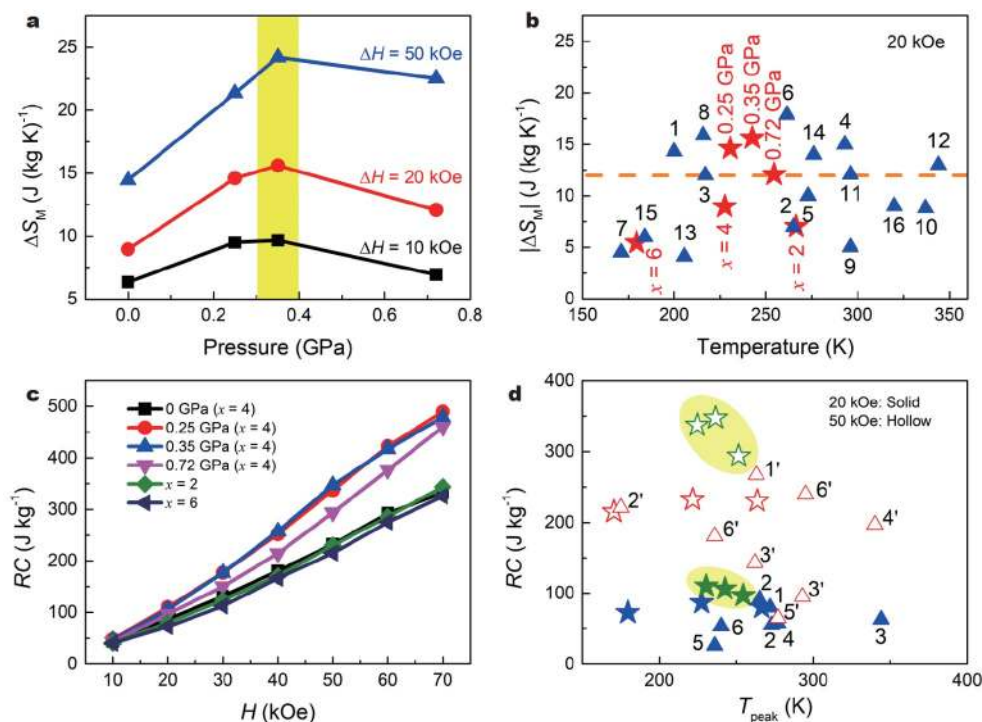
Figure 4 (a) The values of ΔS_M as a function of hydrostatic pressure with magnetic field changes of 10, 20, and 50 kOe, respectively. (b) Comparison of ΔS_M ($\Delta H = 20$ kOe) of the present ribbons with other materials. Red star: present work. Blue triangles: 1, LaFe$_{11.4}$Si$_{1.6}$ [7]; 2, MnNi$_{0.77}$Fe$_{0.23}$Ge [8]; 3, Mn$_{0.64}$Fe$_{0.36}$NiGe$_{0.7}$Si$_{0.3}$ [8]; 4, Mn$_{0.8}$Co$_{0.2}$NiGe$_{0.75}$Si$_{0.25}$ [8]; 5, Ni$_{35}$Co$_{15}$Mn$_{35}$Ti$_{15}$ [19]; 6, Ni$_{36.3}$Co$_{13.7}$Mn$_{35}$Ti$_{15}$ [21]; 7, Ni$_{35}$Co$_{15}$Mn$_{35}$Ti$_{15}$ [21]; 8, Ni$_{35}$Cu$_{2.5}$Co$_{12.5}$Mn$_{35}$Ti$_{15}$ [24]; 9, Ni$_{37}$Co$_9$Fe$_4$Mn$_{35}$Ti$_{15}$ [24]; 10, Ni$_{36.5}$Co$_{13.5}$Mn$_{35}$Ti$_{15}$ [41]; 11, Ni$_{32}$Co$_{18}$Mn$_{35}$Ti$_{15}$ [41]; 12, Ni$_{36.0}$Co$_{14.0}$Mn$_{35.7}$Ti$_{14.3}$ [48]; 13, Ni$_{32}$Fe$_{18}$Mn$_{35}$Ti$_{15}$ [17]; 14, Gd$_5$(Si$_2$Ge$_2$) [49]; 15, Mn-Ni-Sn [50]; 16, MnCo$_{0.958}$Fe$_{0.042}$Ge [46]. (c) Magnetic field dependence of RC using the temperatures at full width half-maximum (FWHM) of the ΔS_M peak as the integration limits under hydrostatic pressures. (d) Comparison of RC (for $\Delta H = 20$ and 50 kOe) of the present ribbons (star) with other materials (triangle). Solid (20 kOe): 1, Ni$_{35}$Co$_{15}$Mn$_{35}$Ti$_{15}$ [19]; 2, Ni$_{50}$Mn$_{34-x}$Cu$_x$In$_{16}$ [51]; 3, Ni$_{36.0}$Co$_{14.0}$Mn$_{35.7}$Ti$_{14.3}$ [48]; 4, Gd$_5$(Si$_2$Ge$_2$) [49]; 5, Ni$_{50}$Mn$_{34.5}$Sn$_{15.5}$ [52]; 6, Ni$_{50}$Mn$_{34}$In$_{16}$ [53]. Hollow (50 kOe): 1', Ni$_{35}$Co$_{15}$Mn$_{35}$Ti$_{15}$ [19]; 2', Ni$_{35-x}$Co$_x$Mn$_{35}$Ti$_{15}$ [41]; 3', Ni$_{50-x}$Co$_x$Mn$_{38}$Sb$_{12}$ [44]; 4', Ni$_{36.0}$Co$_{14.0}$Mn$_{35.7}$Ti$_{14.3}$ [48]; 5', Gd$_5$(Si$_2$Ge$_2$) [49]; 6', Ni$_{50}$Mn$_{34}$In$_{16}$ [53].

under the chemical and hydrostatic pressures. The Fe atoms prefer to occupy Mn(B) sites accompanied by total moments decrease by the first principle calculations. With increasing Fe content, T_t decreases monotonously. With increase of hydrostatic pressure for Ni$_{35}$Co$_{15}$Mn$_{31}$Fe$_4$Ti$_{15}$, T_t increases from 196 K ($P = 0$ GPa) to 236 K ($P = 0.72$ GPa). Therefore, T_t can be tailored jointly by dual-fields (chemical pressure and hydrostatic pressure) in the all-d-metal alloy system. Furthermore, obviously enhanced ΔS_M and RC can also be obtained. The maximum values of ΔS_M and RC reach 15.61(24.20) J (kg K)$^{-1}$ and 109.91 (347.26) J kg^{-1} with $\Delta H = 20(50)$ kOe, respectively. These magnetocaloric performances are superior to most of the recently reported famous materials, indicating the potential application for active MC. The present study would provide useful methods to improve the magnetocaloric performances and tune the MT of the all-d-metal MST alloys.

1 Moya X, Kar-Narayan S, Mathur ND. Caloric materials near ferroic phase transitions. Nat Mater, 2014, 13: 439–450

2 Franco V, Blázquez JS, Ipus JJ, et al. Magnetocaloric effect: From materials research to refrigeration devices. Prog Mater Sci, 2018, 93: 112–232

3 Terada N, Mamiya H. High-efficiency magnetic refrigeration using holmium. Nat Commun, 2021, 12: 1212

4 Zhao C, Zhou L, Zhang Z, et al. Insight of the influence of magnetic-field direction on magneto-plasmonic interfaces for tuning photocatalytical performance of semiconductors. J Phys Chem Lett, 2018, 11: 9931–9937

5 Hu L, Cao L, Li L, et al. Two-dimensional magneto-photoconductivity in non-van der Waals manganese selenide. Mater Horiz, 2021, 8: 1286–1296

6 Hou Z, Li L, Liu C, et al. Emergence of room temperature stable skyrmionic bubbles in the rare earth based REMn$_2$Ge$_2$ (RE = Ce, Pr, and Nd) magnets. Mater Today Phys, 2021, 17: 100341

7 Shen BG, Sun JR, Hu FX, et al. Recent progress in exploring magnetocaloric materials. Adv Mater, 2009, 21: 4545–4564

8 Liu E, Wang W, Feng L, et al. Stable magnetostructural coupling with tunable magnetoresponsive effects in hexagonal ferromagnets. Nat Commun, 2012, 3: 873

9 Mañosa L, González-Alonso D, Planes A, et al. Giant solid-state barocaloric effect in the Ni-Mn-In magnetic shape-memory alloy. Nat Mater, 2010, 9: 478–481

10 Smith A, Bahl CRH, Bjørk R, et al. Materials challenges for high performance magnetocaloric refrigeration devices. Adv Energy Mater, 2012, 2: 1288–1318

11 Zhang Y. Review of the structural, magnetic and magnetocaloric properties in ternary rare earth RE$_2$T$_2$X type intermetallic compounds. J Alloys Compd, 2019, 787: 1173–1186

12 Li L, Yan M. Recent progresses in exploring the rare earth based intermetallic compounds for cryogenic magnetic refrigeration. J Alloys Compd, 2020, 823: 153810

13 Ma Z, Dong X, Zhang Z, et al. Achievement of promising cryogenic magnetocaloric performances in La$_{1-x}$Pr$_x$Fe$_{12}$B$_6$ compounds. J Mater Sci

Tech, 2021, 92: 138–142

14 Zhang Y, Wu B, Guo D, et al. Magnetic properties and promising cryogenic magneto-caloric performances of $Gd_{20}Ho_{20}Tm_{20}Cu_{20}Ni_{20}$ amorphous ribbons. Chin Phys B, 2021, 30: 017501

15 Li L, Xu P, Ye S, et al. Magnetic properties and excellent cryogenic magnetocaloric performances in B-site ordered RE_2ZnMnO_6 (RE = Gd, Dy and Ho) perovskites. Acta Mater, 2020, 194: 354–365

16 Xu P, Ma Z, Wang P, et al. Excellent cryogenic magnetocaloric performances in ferromagnetic Sr_2GdNbO_6 double perovskite compound. Mater Today Phys, 2021, 20: 100470

17 Wu B, Zhang Y, Guo D, et al. Structure, magnetic properties and cryogenic magneto-caloric effect (MCE) in RE_2FeAlO_6 (RE = Gd, Dy, Ho) oxides. Ceramics Int, 2021, 47: 6290–6297

18 Wang Y, Guo D, Wu B, et al. Magnetocaloric effect and refrigeration performance in $RE_{60}Co_{20}Ni_{20}$ (RE = Ho and Er) amorphous ribbons. J Magn Magn Mater, 2020, 498: 166179

19 Wei ZY, Liu EK, Chen JH, et al. Realization of multifunctional shape-memory ferromagnets in all-d-metal Heusler phases. Appl Phys Lett, 2015, 107: 022406

20 Zeng Q, Shen J, Zhang H, et al. Electronic behaviors during martensitic transformations in all-d-metal Heusler alloys. J Phys-Condens Matter, 2019, 31: 425401

21 Wei ZY, Liu EK, Li Y, et al. Magnetostructural martensitic transformations with large volume changes and magneto-strains in all-d-metal Heusler alloys. Appl Phys Lett, 2016, 109: 071904

22 Cong D, Xiong W, Planes A, et al. Colossal elastocaloric effect in ferroelastic Ni-Mn-Ti alloys. Phys Rev Lett, 2019, 122: 255703

23 Aznar A, Gràcia-Condal A, Planes A, et al. Giant barocaloric effect in all-d-metal Heusler shape memory alloys. Phys Rev Mater, 2019, 3: 044406

24 Neves Bez H, Pathak AK, Biswas A, et al. Giant enhancement of the magnetocaloric response in Ni-Co-Mn-Ti by rapid solidification. Acta Mater, 2019, 173: 225–230

25 Liu S, Xuan H, Cao T, et al. Magnetocaloric and elastocaloric effects in all-d-metal $Ni_{37}Co_9Fe_4Mn_{35}Ti_{15}$ magnetic shape memory alloy. Phys Status Solidi A, 2019, 216: 1900563

26 Gottschall T, Bykov E, Gràcia-Condal A, et al. Advanced characterization of multicaloric materials in pulsed magnetic fields. J Appl Phys, 2020, 127: 185107

27 Wei Z, Shen Y, Zhang Z, et al. Low-pressure-induced giant barocaloric effect in an all-d-metal Heusler $Ni_{35.5}Co_{14.5}Mn_{35}Ti_{15}$ magnetic shape memory alloy. APL Mater, 2020, 8: 051101

28 Taubel A, Beckmann B, Pfeuffer L, et al. Tailoring magnetocaloric effect in all-d-metal Ni-Co-Mn-Ti Heusler alloys: A combined experimental and theoretical study. Acta Mater, 2020, 201: 425–434

29 Sanvito S, Oses C, Xue J, et al. Accelerated discovery of new magnets in the Heusler alloy family. Sci Adv, 2017, 3: e1602241

30 Tan JG, Liu ZH, Zhang YJ, et al. Site preference and tetragonal distortion of Heusler alloy Mn-Ni-V. Results Phys, 2019, 12: 1182–1189

31 Ni Z, Guo X, Liu X, et al. Understanding the magnetic structural transition in all-d-metal Heusler alloy $Mn_2Ni_{1.25}Co_{0.25}Ti_{0.5}$. J Alloys Compd, 2019, 775: 427–434

32 Han Y, Wu M, Feng Y, et al. Competition between cubic and tetragonal phases in all-d-metal Heusler alloys, $X_{2-x}Mn_{1+x}V$ (X = Pd, Ni, Pt, Ag, Au, Ir, Co; x = 1, 0): A new potential direction of the Heusler family. IUCrJ, 2019, 6: 465–472

33 Sharma J, Coelho AA, Repaka DVM, et al. Pressure induced martensitic transition, magnetocaloric and magneto-transport properties in Mn-Ni-Sn Heusler alloy. J Magn Magn Mater, 2019, 487: 165307

34 Arumugam S, Ghosh S, Ghosh A, et al. Effect of hydrostatic pressure on the magnetic, exchange bias and magnetocaloric properties of $Ni_{45.5}$-$Co_2Mn_{37.5}Sn_{15}$. J Alloys Compd, 2017, 712: 714–719

35 Samanta T, Lepkowski DL, Saleheen AU, et al. Hydrostatic pressure-induced modifications of structural transitions lead to large enhancements of magnetocaloric effects in MnNiSi-based systems. Phys Rev B, 2015, 91: 020401

36 Devarajan U, Singh S, Muthu SE, et al. Investigations on the electronic transport and piezoresistivity properties of $Ni_{2-x}Mn_{1+x}Ga$ (X = 0 and

0.15) Heusler alloys under hydrostatic pressure. Appl Phys Lett, 2014, 105: 252401

37 Devi P, Mejía CS, Caron L, et al. Effect of chemical and hydrostatic pressure on the coupled magnetostructural transition of Ni-Mn-In Heusler alloys. Phys Rev Mater, 2019, 3: 122401

38 Lázpita P, L'vov VA, Fernández JR, et al. Combined effect of magnetic field and hydrostatic pressure on the phase transitions exhibited by Ni-Mn-In metamagnetic shape memory alloy. Acta Mater, 2020, 193: 1–9

39 Bansil A, Kaprzyk S. First-principles treatment of disorder effects in complex alloys: A study of $Ba_xK_{1-x}BiO_3$ and $BaPb_{1-x}Bi_xO_3$. Phys Rev B, 1991, 43: 10335–10339

40 Qu YH, Cong DY, Li SH, et al. Simultaneously achieved large reversible elastocaloric and magnetocaloric effects and their coupling in a magnetic shape memory alloy. Acta Mater, 2018, 151: 41–55

41 Liu K, Ma S, Ma C, et al. Martensitic transformation and giant magneto-functional properties in all-d-metal Ni-Co-Mn-Ti alloy ribbons. J Alloys Compd, 2019, 790: 78–92

42 Li Y, Huang S, Wang W, et al. Ferromagnetic martensitic transformation and large magnetocaloric effect in $Ni_{35}Co_{15-x}Fe_xMn_{35}Ti_{15}$ (x = 2, 4, 6, 8) alloys. J Appl Phys, 2020, 127: 233907

43 Niculescu V, Burch TJ, Raj K, et al. Properties of Heusler-type materials Fe_2TSi and $FeCo_2Si$. J Magn Magn Mater, 1977, 5: 60–66

44 Nayak AK, Suresh KG, Nigam AK, et al. Pressure induced magnetic and magnetocaloric properties in NiCoMnSb Heusler alloy. J Appl Phys, 2009, 106: 053901

45 Caron L, Ou ZQ, Nguyen TT, et al. On the determination of the magnetic entropy change in materials with first-order transitions. J Magn Magn Mater, 2009, 321: 3559–3566

46 Li Y, Zeng Q, Wei Z, et al. An efficient scheme to tailor the magnetostructural transitions by staged quenching and cyclical ageing in hexagonal martensitic alloys. Acta Mater, 2019, 174: 289–299

47 Banerjee BK. On a generalised approach to first and second order magnetic transitions. Phys Lett, 1964, 12: 16–17

48 Liu K, Han X, Yu K, et al. Magnetic-field-induced metamagnetic reverse martensitic transformation and magnetocaloric effect in all-d-metal $Ni_{36.0}Co_{14.0}Mn_{35.7}Ti_{14.3}$ alloy ribbons. Intermetallics, 2019, 110: 106472

49 Pecharsky VK, Gschneidner KA. Giant magnetocaloric effect in $Gd_5(Si_2Ge_2)$. Phys Rev Lett, 1997, 78: 4494–4497

50 Krenke T, Duman E, Acet M, et al. Inverse magnetocaloric effect in ferromagnetic Ni-Mn-Sn alloys. Nat Mater, 2005, 4: 450–454

51 Kaya M, Yildirim S, Yüzüak E, et al. The effect of the substitution of Cu for Mn on magnetic and magnetocaloric properties of $Ni_{50}Mn_{34}In_{16}$. J Magn Magn Mater, 2014, 368: 191–197

52 Babita I, Patil SI, Ram S. First order structural transformation and inverse magnetocaloric effect in melt-spun Ni-Mn-Sn ribbons. J Phys D-Appl Phys, 2010, 43: 205002

53 Sharma VK, Chattopadhyay MK, Roy SB. Large inverse magnetocaloric effect in $Ni_{50}Mn_{34}In_{16}$. J Phys D-Appl Phys, 2007, 40: 1869–1873

Author contributions Li Y designed and fabricated the samples; Qin L and Huang S performed the experiments and processed the data; Li Y prepared the manuscript. All the authors contributed to the discussion and review and editing. Li L contributed to the conceptualization and supervision.

Conflict of interest The authors declare that they have no conflict of interest.

Supplementary information Supporting data are available in the online version of the paper.

Yong Li received his PhD degree in materials science and engineering from Hebei University of Technology in 2018. He is currently a research assistant at Hangzhou Dianzi University. His research interests are novel functional materials with magnetic phase transitions, including magnetic-field-driven martensitic transformation, magnetic shape memory alloys, and magnetocaloric effect materials.

Lingwei Li received his PhD degree at the University of Toyama (Japan). He was granted by the Japan Society for the Promotion of Science (JSPS) and Alexander von Humboldt (AvH) scholarship for the postdoctoral research. Currently, he is a professor at Hangzhou Dianzi University, director of the Key Laboratory of Novel Materials for Sensor of Zhejiang Province. He has been selected as one of the highly cited Chinese researchers 2020 by Elsevier as well as world's top 2% scientists 2020 by Stanford University. His research interests mainly include magnetism and magnetic materials as well as rare-earth-based functional materials.

化学压和等静压调控全过渡族Heusler合金Ni$_{35}$Co$_{15}$-Mn$_{35-x}$Fe$_x$Ti$_{15}$的磁热效应和马氏体相变

李勇, 覃亮, 黄思源, 李领伟*

摘要 基于磁热效应的固态磁致冷方式被认为是一种环境友好且高能效的技术. 探索和设计具有大磁热效应的固态磁致冷材料是目前的研究重点之一. 本文通过在Ni$_{35}$Co$_{15}$Mn$_{35-x}$Fe$_x$Ti$_{15}$中引入化学压和等静压, 在理论和实验上对其晶体结构、马氏体相变和磁热性能进行了研究. 结果表明, 室温下, 样品呈现B2相结构, Fe原子倾向于占Mn(B)位. Fe含量降低、晶胞体积收缩均能导致总磁矩的降低. 马氏体相变温度随Fe含量增加而降低, 随等静压增强而升高. 此外, 施加等静压可获得显著增强的磁热效应. 在0–20(0–50) kOe场下, 最大磁熵变值(ΔS_M^{max})和制冷能力(RC)分别达到15.61(24.20) J (kg K)$^{-1}$和109.91(347.26) J kg^{-1}. 该数值优于最近报道的多数磁致冷材料, 表明Ni$_{35}$Co$_{15}$Mn$_{35-x}$Fe$_x$Ti$_{15}$体系有望成为固态磁致冷备选材料之一.